Nanoscale Advances

ROYAL SOCIETY OF CHEMISTRY

PAPER

View Article Online
View Journal | View Issue

Cite this: *Nanoscale Adv.*, 2024, **6**, 2407

Photoelectrochemical performance of a nanostructured $BiVO_4$/NiOOH/FeOOH–Cu_2O/CuO/TiO_2 tandem cell for unassisted solar water splitting†

S. R. Sitaaraman,[ab] A. Nirmala Grace,[a] Jiefang Zhu[c] and Raja Sellappan*[a]

An unassisted solar water splitting tandem cell is fabricated using FeOOH/NiOOH-coated $BiVO_4$ nanostructures as a photoanode and a TiO_2-protected heterojunction Cu_2O/CuO thin film as a photocathode. The individual photoelectrochemical (PEC) performance of the nanostructured $BiVO_4$/NiOOH/FeOOH photoanode produces a photocurrent of 2.05 mA cm^{-2} at 1.23 V *vs.* RHE, while the Cu_2O/CuO/TiO_2 photocathode delivers −1.61 mA cm^{-2} at 0 V *vs.* RHE under an AM 1.5 filtered illumination of 100 mW cm^{-2}. The operating point of tandem cell photocurrent is found to be 0.273 mA cm^{-2} at 0.56 V *vs.* RHE. From two-electrode linear sweep voltammetry, the tandem cell ($BiVO_4$/NiOOH/FeOOH–Cu_2O/CuO/TiO_2) delivers an unassisted current density of 0.201 mA cm^{-2} at 0 V. The chronoamperometry test further demonstrates the stable nature of the tandem cell, which retains a current density of 0.187 mA cm^{-2} during a testing duration of 3000 seconds. The proposed tandem cell provides optimized solutions to designing a cost-effective and stable solar water splitting system for the fulfillment of the future energy needs.

Received 29th January 2024
Accepted 15th March 2024

DOI: 10.1039/d4na00088a

rsc.li/nanoscale-advances

1. Introduction

The production of solar hydrogen using semiconductor photoelectrode materials is considered a potential strategy to provide clean and green energy with zero carbon footprint without substantially modifying the existing infrastructure. A single-electrode semiconductor photoelectrochemical (PEC) system has yet to find a way to achieve a practical efficiency of 10% since the pioneering work of Fujishima and Honda in 1972.[1] The tandem integration of solar cells along with the PEC system[2] is advantageous when state-of-the-art solar cells are constructed with semiconductor materials for solar water splitting. Recent research studies examined such an approach by combining photovoltaic devices, such as dye sensitized solar cells[3] and perovskite solar cells,[4] with a PEC device consisting of a single semiconductor electrode and found that it produces a higher solar-to-hydrogen (STH) conversion efficiency (13.8%).[5] However, the overall complexity of the system and photocorrosion of narrow bandgap semiconductors are critical issues in commercializing such approaches. Compared to the PV-integrated PEC approach, a tandem PEC cell consisting of an n-type photoanode and p-type photocathode[6] is a viable approach in terms of feasibility and practicality. Certain basic requirements should be met for the construction of efficient tandem PEC cells. First, the bandgap of semiconductors used in tandem cells should be complementary to each other and should be chosen as per the proposed contour plot[7] to achieve the maximum theoretical efficiency. The implementation of complementary bandgap semiconductors enables harvesting a significant portion of the incoming solar spectrum.[8] Second, the valence band edge position of the semiconductor should be more positive than the water oxidation potential (1.23 V *vs.* RHE at pH = 0) for photoanodes, and the conduction band edge of the semiconductor should be more negative than the water reduction potential (0 V *vs.* RHE at pH = 0) for photocathodes.[9] The difference in the Fermi level of the photoanode and photocathode determines the bias required for solar water splitting.

Among various semiconductors, bandgap tunable ternary metal oxides are suitable candidates for photoanodes.[10] $BiVO_4$ fulfills several requirements of being an efficient photoanode in a tandem cell. With a bandgap of 2.4 eV (ref. 11) and favorable band edge positions, $BiVO_4$ can be used for the water oxidation reaction. However, $BiVO_4$ suffers from surface recombination, a high onset potential and poor water oxidation kinetics.[12] These hurdles significantly reduce the current density of $BiVO_4$

[a]*Centre for Nanotechnology Research, Vellore Institute of Technology, Vellore, India-632014. E-mail: raja.sellappan@vit.ac.in*

[b]*Department of Electrical and Electronics Engineering, SRM Institute of Science and Technology, Ramapuram, Chennai, India-600089*

[c]*Department of Chemistry – Ångström Laboratory, Uppsala University, 75121 Uppsala, Sweden*

† Electronic supplementary information (ESI) available. See DOI: https://doi.org/10.1039/d4na00088a

compared to the theoretical current density of 7.5 mA cm^{-2}.[13] Approaches, such as the addition of dopants, heterojunction formation, incorporating an interlayer[14] and increasing the surface area by morphology control, can improve its PEC properties. $BiVO_4$ porous nanostructures help in aiding the charge separation and surface-to-volume ratio due to its hollow network. Sutripto Majumder *et al.*[15] studied the effect of $ZnFe_2O_4$ on $BiVO_4$ nanostructure photoanodes, which produced a photocurrent density of 0.73 mA cm^{-2} at 1.23 V *vs.* RHE. This photocurrent density value is higher than that for the thin film counterpart.[16] In order to obtain unassisted tandem cell operation, the onset potential could be reduced or the current density should be increased in the lower applied potential region.[17] To achieve this, the co-catalyst can be loaded onto the surface of the photoanode. The loading of the oxygen evolution reaction (OER) co-catalysts provides active sites for the interfacial reaction, in addition to reducing the overpotential. The OER catalysts also improve the stability by effectively transferring the photogenerated carriers from the bulk of the photoanode to the surface due to the favorable band alignment. Several inexpensive transition metal oxyhydroxides such as FeOOH and NiOOH have been extensively used as co-catalysts for the $BiVO_4$ photoanode. Dong Ki Lee *et al.*[18] analyzed the effect of $BiVO_4$ using dual oxyhydroxides, which produced a remarkable current density of ~5 mA cm^{-2} at 1.23 V *vs.* RHE.

Among various photocathode materials, cuprous oxide (Cu_2O) fulfills many requirements, such as a narrow bandgap, ease of fabrication and suitable band edge positions. The narrow bandgap of 2.1 eV is capable of boosting the efficiency of the tandem cells. On the other hand, Cu_2O suffers from higher recombination, owing to the short diffusion length of the minority charge carriers and photocorrosion in the presence of an aqueous medium. The film thickness of 1 μm is required for effective absorption, but the achieved diffusion length ranges from 20 to 200 nm based on the synthesis process.[19] Charge separation is also a crucial parameter to maximize the performance of the photocathode in the tandem cell. Cupric oxide (CuO) is comparatively more stable than Cu_2O. Appropriate band matching of Cu_2O and CuO boosts the performance of the photocathode.[20] The heterojunction of Cu_2O and CuO showed promising PEC performance in terms of the stability, charge separation and efficiency. Pan Wang *et al.*[21] constructed a Pt-loaded Cu_2O/CuO heterojunction photocathode, which produced a current density of −1.99 mA cm^{-2} at the water reduction potential. The increase in the current density was attributed to improved charge separation due to *in situ* formation of the CuO layer. The addition of the CuO layer reduced the charge transfer barrier at the surface. To prevent photocorrosion, various protective layers, such as TiO_2 and carbon,[22] can be deposited. Yuanbin Wang *et al.* demonstrated a TiO_2 protective layer on the Cu_2O photocathode using the atomic layer deposition method (ALD), which generated a current density of −3.71 mA cm^{-2} at 0 V *vs.* RHE. A band alignment of Cu_2O/CuO provides stable protection with better charge separation and transport.[23]

In this work, we constructed a model tandem system consisting of a nanostructured $BiVO_4$/NiOOH/FeOOH photoanode and Cu_2O/CuO/TiO_2 photocathode towards enhancing the PEC performance of the cell for unassisted solar water splitting. The novelty of this tandem cell is the employment of earth-abundant oxide semiconductor materials, which is chemically more stable than non-oxide elemental semiconductors. The combination of the photoelectrodes and inexpensive co-catalysts has rarely been reported in the literature in terms of the nanostructured photoanode and heterojunction photocathodes with a protective layer. We anticipate that the tandem cell will simultaneously improve the optical absorption, charge transport, and interfacial charge transfer for unbiased solar water splitting. The nanostructured photoanode enhanced the surface area, and the NiOOH/FeOOH dual layer co-catalysts minimized the overpotential and improved the charge transfer resistance. The performance of the photocathode was improved through heterojunction formation with stable CuO on Cu_2O. The photocathode was further deposited by a spin-coated TiO_2 layer to protect it from photocorrosion. The constructed $BiVO_4$/NiOOH/FeOOH photoanode-Cu_2O/CuO/TiO_2 photocathode produced a positive current density in the unassisted PEC tests. The non-zero operating points provided the possibility of the operation of a tandem cell without an external bias.

2. Experimental methods

2.1 Materials

Bismuth nitrate pentahydrate, *p*-benzoquinone, copper sulphate pentahydrate, FTO substrates, iron sulphate, and potassium iodide were purchased from Sigma Aldrich. Lactic acid and vanadyl acetylacetonate were purchased from Avra chemicals. Nickel sulphate hexahydrate and sodium hydroxide were purchased from SDFCL limited. Sodium sulphate was purchased from Alfa Aesar. All of the chemicals used in the study were of analytical grade, and used without further purification.

2.2 Preparation of $BiVO_4$ nanostructures

FTO substrates were separately ultrasonically cleaned with acetone, isopropanol and ethanol. The $BiVO_4$ photoanodes were prepared through the electrodeposition of BiOI on FTO substrates, followed by the conversion of BiOI into $BiVO_4$ using the drop-casting of a vanadium precursor solution and subsequent annealing in air.[24]

2.2.1 Electrochemical deposition of BiOI. The electrodeposition of bismuth oxyiodide (BiOI) was performed in a typical three-electrode setup, in which the FTO substrate, Ag/AgCl (saturated KCl) and platinum (Pt) wire were used as the working, reference and counter electrodes, respectively. FTO substrates were ultrasonically cleaned using acetone, isopropanol and ethanol sequentially. The plating solution consists of 15 mM of bismuth nitrate pentahydrate, 400 mM of potassium iodide, and 30 mM lactic acid. The precursors were rigorously stirred to make a clear homogenous solution, and the pH was adjusted to 1.8 by adding dilute nitric acid. First, 46 mM of *p*-benzoquinone was mixed in 20 mL ethanol. Then, the *p*-benzoquinone solution was added to the bismuth nitrate

solution slowly because the sudden addition can cause precipitation of BiOI. The plating solution was stirred for 10 minutes, and the pH was adjusted to 3.4 using dilute nitric acid. The electrochemical deposition of BiOI on the FTO substrates was carried out by applying a constant potential of −0.3 V *vs.* Ag/AgCl for 20 seconds to increase the nucleation density, followed by applying a constant potential of −0.1 V *vs.* Ag/AgCl for various time periods (2.5, 5, 7.5 and 10 minutes) to obtain an optimum coating. Finally, BiOI films were rinsed with DI water and dried at room temperature.

2.2.2 Conversion of BiOI into $BiVO_4$ photoanodes. After the electrodeposition of BiOI, the substrates were drop-casted with 200 mM of vanadyl acetylacetonate in dimethyl sulphoxide (DMSO). The substrates were subsequently transferred to a box furnace for thermal treatment at 450 °C for 2 hours in air. After formation of the $BiVO_4$ nanostructures, the excess V_2O_5 formed during the thermal treatment was removed by soaking the $BiVO_4$ photoanode in 1 M NaOH solution for 30 minutes with stirring at 200 rpm. After this process, the $BiVO_4$ photoanodes were rinsed with a copious amount of DI water and dried at room temperature.

2.3 Deposition of FeOOH and NiOOH co-catalysts

The dual co-catalysts were deposited using an electrodeposition method.[25,26] The electrodeposition procedure was carried out in a three-electrode system, in which the $BiVO_4$ photoanode, Ag/AgCl saturated KCl, and Pt wire were the working electrode, reference electrode, and counter electrode, respectively. Briefly, 0.1 M of iron sulphate solution was prepared and a constant potential of 1.2 V was applied for 5 minutes. The photoanode was rinsed with DI water and dried at room temperature. Similarly, for NiOOH deposition, 0.1 M nickel sulphate solution was prepared and a constant potential of 1.2 V was applied for 5 minutes. Finally, the photoanode was rinsed with DI water and dried at room temperature.

2.4 Preparation of the Cu_2O and Cu_2O/CuO photocathodes

The Cu_2O photocathode was prepared using an electrodeposition method.[27] The Cu_2O plating solution consisted of 0.4 M copper sulphate pentahydrate in 3 M lactic acid. A constant potential of −0.4 V *vs.* Ag/AgCl was applied to deposit Cu_2O on the FTO substrate for an hour. Finally, Cu_2O deposited on the FTO substrates was rinsed with a copious amount of DI water and dried at room temperature.

For the *in situ* growth of CuO on Cu_2O, the prepared Cu_2O photocathode was annealed at 300 °C, 400 °C and 500 °C for 30 minutes in an air environment using a muffle furnace.[28]

2.5 Preparation of the TiO_2 protective layer

The deposition of TiO_2 was performed using a spin-coating technique.[29] The TiO_2 precursor sol was prepared by mixing titanium isopropoxide in isopropanol (1 : 50 volume ratio). The prepared sol was spin-coated at 1000 rpm for 30 seconds. The TiO_2-coated Cu_2O/CuO photocathode (Cu_2O/CuO/TiO_2) was annealed at 200 °C for 1 hour in ambient air.

2.6 Material characterization

The structural characterization was performed using an X-ray diffractometer, D8 Advanced, Bruker with Cu-Kα radiation (λ = 1.5418 Å). Vibrational characterization was carried out using the Raman microscope, Horiba XploRA™ plus with the 532 nm green laser as a source (25% laser power). The morphology of the photoanode was analysed using a field emission scanning electron microscope (FESEM), FEI Quanta 250 FEG. Optical characterization was carried out using a UV-vis spectrometer, Specord Plus in the visible range.

2.7 Photoelectrochemical characterization

All of the photoelectrochemical (PEC) characterization was carried out in a 3-electrode setup with the photoanode/photocathode as the working electrode, Ag/AgCl saturated KCl as the reference electrode, and Pt wire as the counter electrode. The PEC characterization was recorded in the AMETEK PARSTAT electrochemical workstation. The illumination source was 300 W ozone-free xenon lamp (Ushio, Japan) from Holmarc, India. The illumination source was adjusted to a power intensity of 100 mW cm^{-2} using a Newport AM 1.5 G filter. The active area of all photoanodes/photocathode was 1 cm^2. All PEC measurements were performed in 0.1 M Na_2SO_4 (pH 6). The electrolyte was purged with nitrogen gas for 30 minutes prior to the testing. All of the PEC measurements were recorded with backside illumination. Linear sweep voltammetry (LSV), chronoamperometry (*j vs. t*), and electrochemical impedance spectroscopy (EIS) and Mott–Schottky analysis were performed to characterize the PEC performance of the photoelectrodes. LSV scans were performed at the scan rate of 20 mV s^{-1}. Current *vs.* time (*j vs. t*) measurements were performed at 1.23 V *vs.* RHE and 0 V *vs.* RHE for the photoanodes and photocathodes, respectively. EIS was performed in the frequency range of 10^5 Hz to 1 Hz using an AC signal with 10 mV amplitude. The Mott–Schottky plot was obtained at a scan range near the reported flat band potential. The potential of the working electrode was converted to a reversible hydrogen electrode (RHE) using the formula, $E_{RHE} = E_{Ag/AgCl} + 0.059 \times pH + E^{\circ}_{Ag/AgCl}$, where $E^{\circ}_{Ag/AgCl}$ is the standard potential of the Ag/AgCl saturated KCl reference electrode, which is 0.197 V. All of the potential in the PEC measurement was reported in the RHE scale.

2.8 Tandem cell PEC measurements

A tandem PEC cell was constructed with $BiVO_4$ nanostructure photoanodes as the top cell and Cu_2O/CuO/TiO_2 as the bottom cell. The tandem measurements were performed in 0.1 M Na_2SO_4 (pH 6) electrolyte. The electrolyte was purged with nitrogen for 30 minutes prior to the experiments. The active area of the photoanode/photocathode was 1 cm^2. Electrochemical analysis, such as linear sweep voltammetry (LSV) and unassisted stability tests (*j vs. t*), was performed.

3. Results and discussion

3.1 Characterization of the photoelectrode materials

Fig. 1(a) and (b) shows the FESEM micrograph of the $BiVO_4$ nanostructured photoanodes with and without co-catalysts.

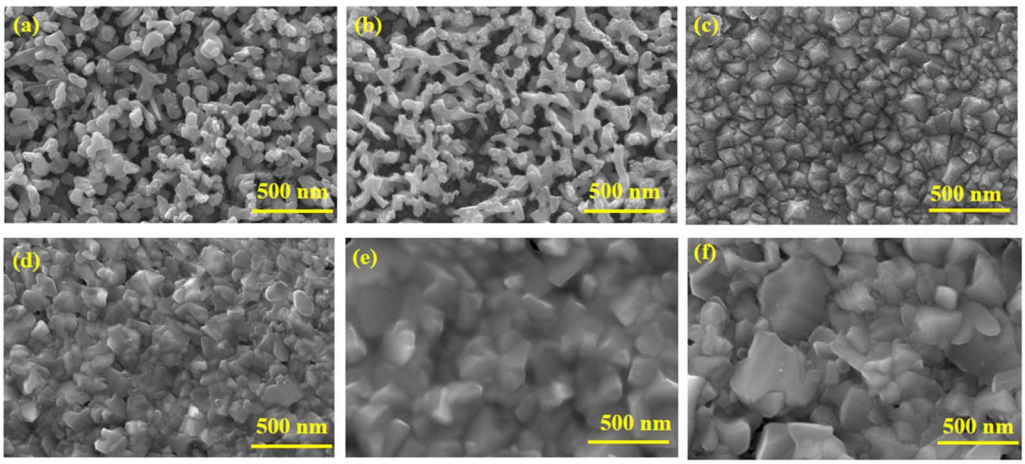

Fig. 1 FESEM image of (a) $BiVO_4$, (b) $BiVO_4$/NiOOH/FeOOH nanostructured photoanodes, (c) pure Cu_2O, (d) Cu_2O/CuO, (e) Cu_2O/CuO/TiO_2 and (f) CuO photocathode.

$BiVO_4$ exhibited a 3D porous network that was formed by small nanoworm-like particles. No significant changes in the morphology was observed after the deposition of NiOOH and FeOOH. Nevertheless, the co-catalyst deposition was confirmed by EDAX elemental analysis (see ESI, Fig. S2†). The electrodeposited Cu_2O in Fig. 1(c) exhibits a dense compact structure. After annealing, the top layer Cu_2O was converted into CuO, and its morphology revealed a slightly bigger dense structure (Fig. 1(f)). As the annealing time (45 minutes) was increased, the Cu_2O layers became completely converted to CuO. Hence, the annealing time was limited to 30 minutes to obtain an optimum Cu_2O/CuO heterojunction, as shown in Fig. 1(d). The cross-sectional FESEM micrograph of the $BiVO_4$/NiOOH/FeOOH nanostructures (2.9 μm thick) and Cu_2O/CuO/TiO_2 (1.176 μm thick) are shown in Fig. S1 (a) and (b) in the ESI,† respectively. Fig. 1(e) shows the protective layer coating of TiO_2 on Cu_2O. It was observed that TiO_2 was conformally coated on top of Cu_2O/CuO (Fig. 1(e)). The corresponding EDS mapping of the $BiVO_4$ nanostructure photoanodes and Cu_2O photocathodes are shown in Fig. S2 and S3 in the ESI,† respectively.

X-Ray Diffraction (XRD) was used to analyze the crystallinity of the photoelectrodes. The XRD pattern of $BiVO_4$ and the modified $BiVO_4$ photoanodes are shown in Fig. 2(a). The peaks at 18.9° and 28.9° confirmed the presence of the monoclinic scheelite structures of $BiVO_4$. The obtained diffraction peaks are well indexed with JCPDS card no. 14-06888.[30] The peaks of the FTO substrate were denoted as '*' since some of the uncoated areas of the substrate were also exposed during the characterization. The remaining XRD peaks in Fig. 2(a) indicated the formation of monoclinic $BiVO_4$. No diffraction peaks were obtained for FeOOH and NiOOH because of the low content and the amorphous nature of the co-catalysts. The XRD patterns of Cu_2O, Cu_2O/CuO and Cu_2O/CuO/TiO_2 are shown in Fig. 2(b). The obtained peaks at 29.8° and 38° are attributed to the formation of cubic Cu_2O. Annealing of the Cu_2O film in air at 400 °C initiated the formation of CuO. The formation of CuO was confirmed by the peaks at 35.5° (002). The annealing duration of 30 minutes indicated a successful formation of Cu_2O to CuO. The XRD pattern obtained with a mixture of Cu_2O and CuO reflects the formation of cubic CuO (indicated in

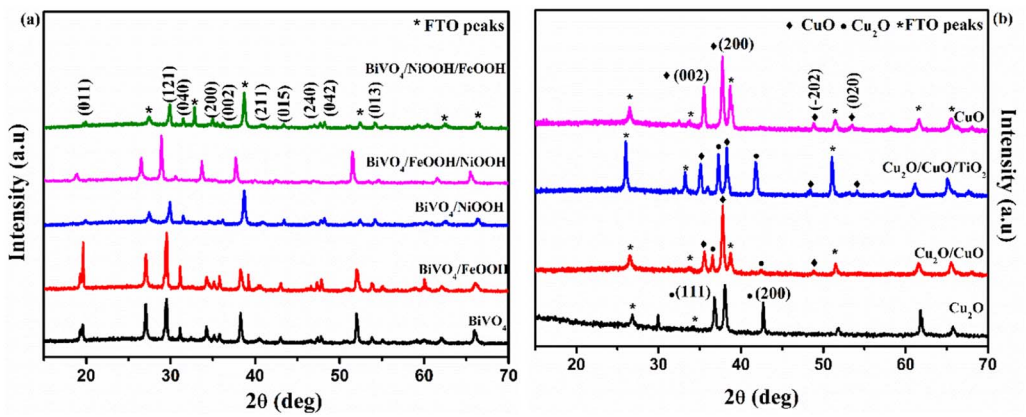

Fig. 2 XRD pattern of (a) $BiVO_4$, $BiVO_4$/FeOOH, $BiVO_4$/NiOOH, $BiVO_4$/FeOOH/NiOOH and $BiVO_4$/NiOOH/FeOOH nanostructured photoanodes and (b) Cu_2O, Cu_2O/CuO, Cu_2O/CuO/TiO_2 and CuO photocathodes.

Fig. 2(b), blue line pattern). The obtained XRD pattern was well indexed with the JCPDS card no. 03-0898 (ref. 20) for Cu_2O and 48-1548 for CuO.[31] No diffraction peak of TiO_2 was obtained for the photocathode because of the low content of the TiO_2 protective layer.

The Raman spectra shown in Fig. 3(a) further confirmed the formation of the $BiVO_4$ photoanode and Cu_2O photocathode. The Raman spectra of the $BiVO_4$ nanostructures proved the formation of the monoclinic scheelite $BiVO_4$ exhibiting the external mode vibration, symmetric and asymmetric deformation of VO_4^{3-} and symmetric stretch mode of V–O at 207.79 cm^{-1}, 324.06 cm^{-1}, 369.52 cm^{-1} and 819.78 cm^{-1}, respectively.[32] The deposition of FeOOH and NiOOH has no effect on the Raman spectra because of the low content of the dual layer co-catalysts. Similarly, Fig. 3(b) proved the formation of Cu_2O photocathodes and the mixed phase formation of Cu_2O/CuO. The second order Raman peak of cubic Cu_2O was ascertained by the sharp peak at 207.05 cm^{-1}. The peak at 293.96 cm^{-1} confirmed the presence of CuO in the Cu_2O/CuO and Cu_2O/CuO/TiO_2 photocathodes. The sharp peak at 207.05 cm^{-1} (peak of Cu_2O) was absent for the pure CuO sample.[33] The significance of the peaks of the $BiVO_4$ photoanode and Cu_2O photocathodes are summarized in Table S1 in the ESI.†

Optical absorption properties are essential in understanding the electronic structure of photocatalysts, which further determines the bandgap of materials. In order to evaluate the optoelectronic properties, UV-vis absorption spectra were measured. Fig. 4(a) shows the absorbance spectra of the $BiVO_4$ nanostructured photoanode. The absorption edge of the photoanodes started at around 550 nm. The absorption edge of Cu_2O was observed at around 700 nm, shown in Fig. 4(c). Upon the formation of CuO on Cu_2O after annealing, the formed heterojunction red-shifted the absorption edge to around 850 nm due to the presence of CuO on the top surface. After thermal oxidation, the top surface of the photocathode was changed from reddish yellow to black, which implies the formation of CuO. The color of the Cu_2O layer was still visible, when the photocathode was viewed from the back side of the conducting substrate. The bandgap was calculated using the absorption spectra from the Tauc's plot shown in Fig. 4(b) and (d). The values of the absorption edge and the band gap of the $BiVO_4$ photoanodes and Cu_2O photocathodes are summarized in Table S2 in the ESI.†

3.2 Photoelectrochemical (PEC) properties

The individual PEC performance of the photoelectrodes were analyzed using a three-electrode setup in 0.1 M Na_2SO_4 electrolyte (pH = 6) under AM 1.5 G illumination, and the results are shown in Fig. 5. From Fig. 5(a), the bare $BiVO_4$ nanostructured photoanode provided an anodic response upon illumination, and produced a photocurrent density of 0.65 mA cm^{-2} at 1.23 V *vs.* RHE. The onset potential of the bare $BiVO_4$ nanostructure photoanode was 0.45 V *vs.* RHE. The $BiVO_4$/FeOOH and $BiVO_4$/NiOOH photoanode achieved an improved photocurrent density of 1.24 and 0.91 mA cm^{-2} at 1.23 V *vs.* RHE, and exhibited a considerable cathodic shift in the onset potential (0.41 V *vs.* RHE). The cathodic shift in the onset potential was ascribed to the reduced surface recombination and accelerated oxygen evolution reaction. The result verifies that the FeOOH and NiOOH co-catalysts effectively collect the

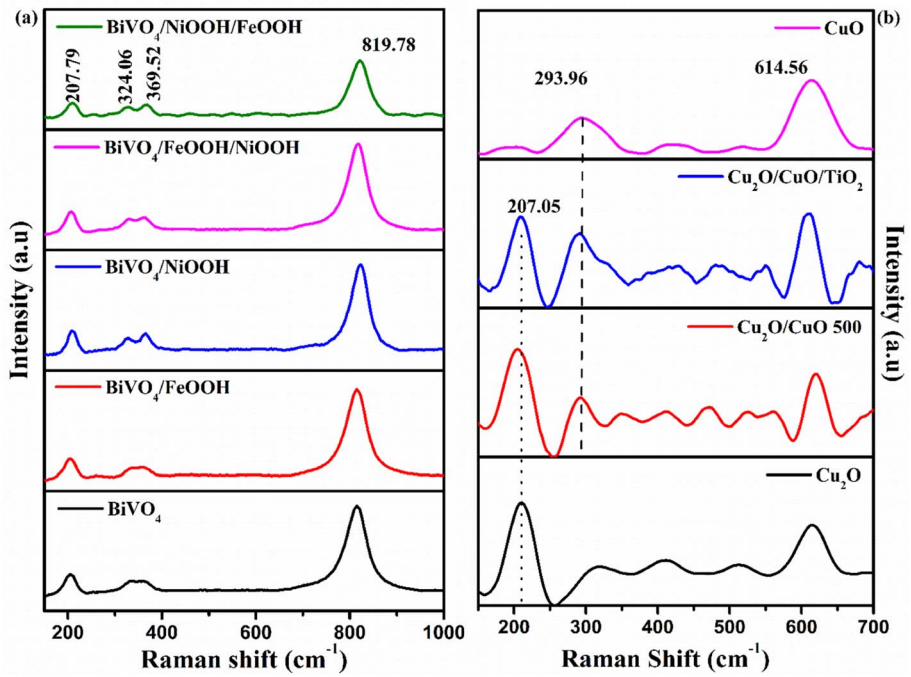

Fig. 3 (a) Raman vibrational spectra of (a) $BiVO_4$, $BiVO_4$/FeOOH, $BiVO_4$/NiOOH, $BiVO_4$/FeOOH/NiOOH and $BiVO_4$/NiOOH/FeOOH nanostructured photoanodes and (b) Cu_2O, Cu_2O/CuO, Cu_2O/CuO/TiO_2 and CuO photocathodes.

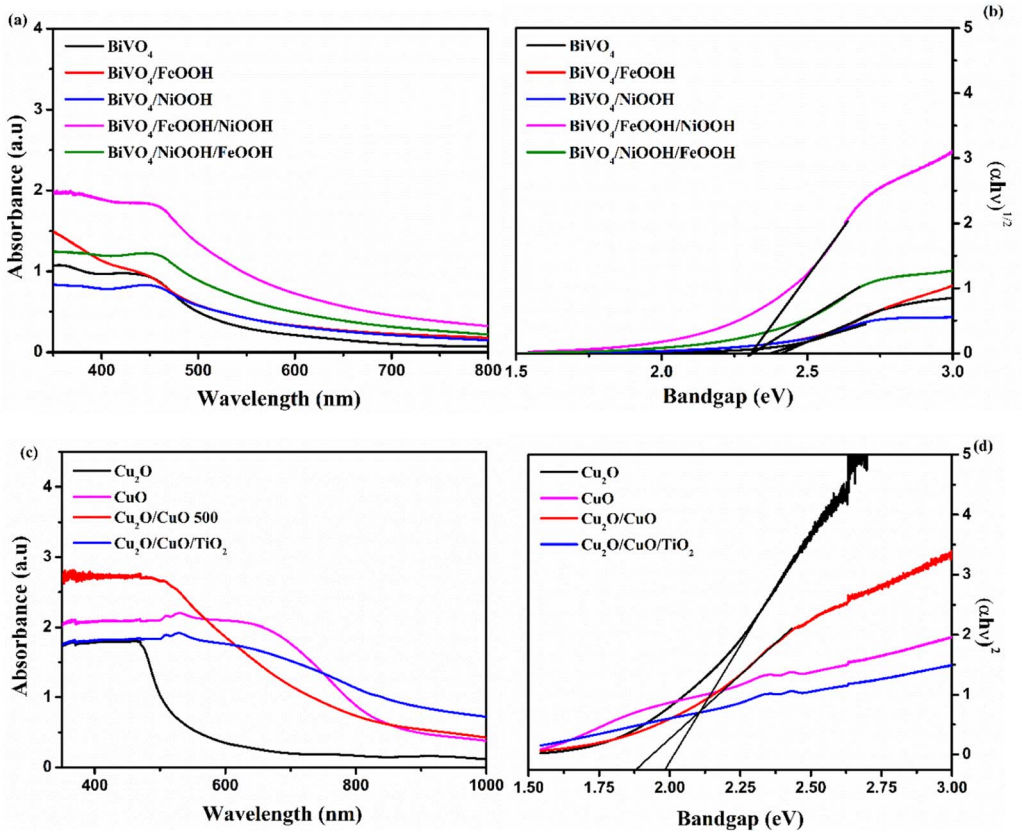

Fig. 4 (a and c) UV-vis absorption spectra. (b and d) Tauc's plot of $BiVO_4$, $BiVO_4$/FeOOH, $BiVO_4$/NiOOH, $BiVO_4$/FeOOH/NiOOH and $BiVO_4$/NiOOH/FeOOH nanostructured photoanodes and Cu_2O, Cu_2O/CuO, (inset) Cu_2O/CuO/TiO_2 and CuO photocathodes.

photogenerated charge carriers for the water oxidation reaction. The combination of both FeOOH and NiOOH co-catalysts on $BiVO_4$ significantly boosted the photocurrent density compared to the individual co-catalyst. The significant enhancement in the photocurrent density and the reduction in the onset potential could be due to the synergic effect of the dual layer co-catalyst configuration. The $BiVO_4$/NiOOH interface minimizes the recombination, while the FeOOH/electrolyte interface enables the surface charge to be more favorable for improving the water oxidation reaction. Chronoamperometry (*j vs. t*) measurements of the $BiVO_4$ nanostructured photoanodes shown in Fig. 5(b) were performed at 1.23 V *vs.* RHE for 140 seconds, and the illumination was chopped for every 20 seconds. The $BiVO_4$/NiOOH/FeOOH photoanode produced a stable photocurrent density of 1.90 mA cm^{-2} for the entire 140 seconds duration.

The PEC performance of the photocathode is shown in Fig. 5(c). As seen from the figure, all photocathodes produced a cathodic response upon illumination, indicating the intrinsic p-type nature of the photoelectrodes. In our previous works, we chose Cu_2O as photocathodes with protective layers in the tandem structure, which produced a decent photocurrent density.[34,35] In this work, a heterojunction of Cu_2O/CuO has been chosen with the TiO_2 protective layer to improve the charge separation and minimize the photocorrosion. The bare Cu_2O and CuO photocathode produced photocurrent densities of −0.62 and −0.81 mA cm^{-2} at 0 V *vs.* RHE, respectively. On the other hand, the Cu_2O/CuO thin film heterojunction structure produced an enhanced photocurrent density of −1.26 mA cm^{-2} at 0 V *vs.* RHE, which is higher than the bare Cu_2O and CuO thin films. The results proved that the heterojunction structure helped in facilitating charge separation due to favorable band alignment at the interface of Cu_2O/CuO and electrolyte. As a result, an improved photocurrent was achieved for this structure. The heterojunction structure was further protected with a thin TiO_2 layer, and the representative Cu_2O/CuO/TiO_2 thin film photocathode achieved the highest photocurrent density of −1.61 mA cm^{-2} at 0 V *vs.* RHE among all prepared photocathodes. The increased onset potential and enhanced photocurrent density were attributed to protection of TiO_2 and the charge separation by the heterojunction structure. The *j vs. t* measurement of the Cu_2O photocathode was performed at 0 V *vs.* RHE for 140 seconds, as shown in Fig. 5(d). It is clearly visible that the Cu_2O/CuO/TiO_2 photocathode produced a stable current density of 1.60 mA cm^{-2} for the entire measurement duration. Table 1 presents the summarized PEC results of the photoelectrodes.

The photostability of the $BiVO_4$ *vs.* $BiVO_4$/NiOOH/FeOOH photoanode and Cu_2O *vs.* Cu_2O/CuO/TiO_2 photocathode was measured at 1.23 V *vs.* RHE and 0 V *vs.* RHE, respectively, for 2000 seconds. From Fig. S5 (a),† it was observed that the addition of the dual-layered electrocatalyst produced a stable

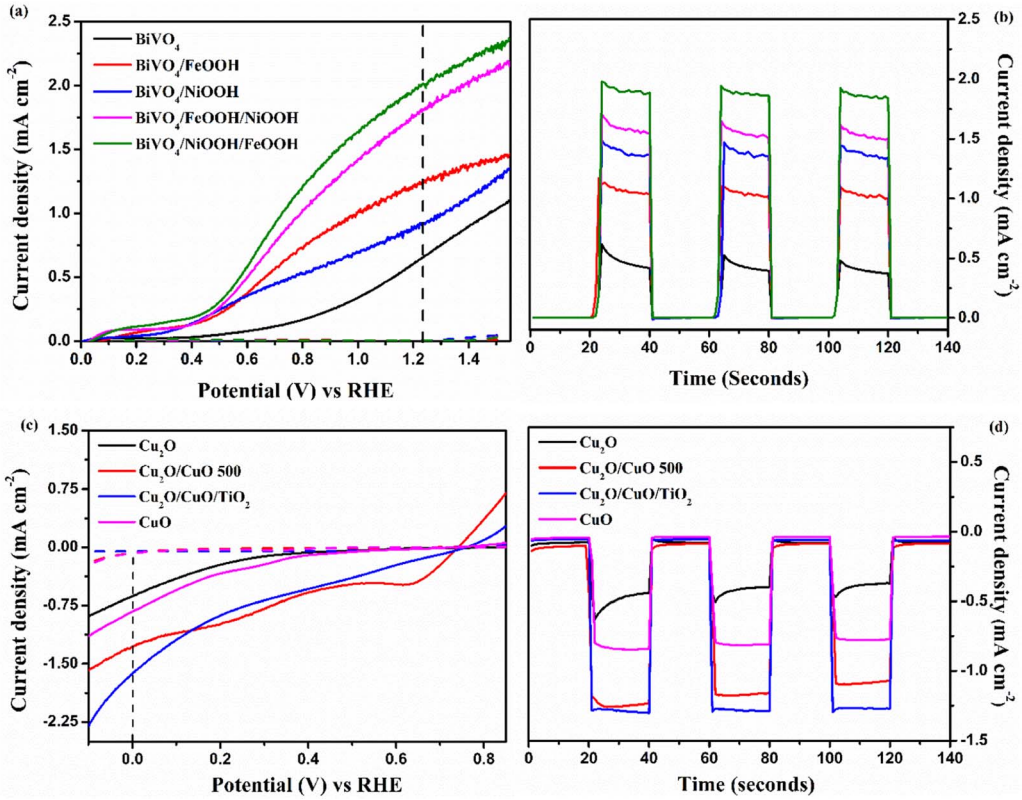

Fig. 5 (a and c) Linear sweep voltammetry (LSV) response of $BiVO_4$, $BiVO_4$/FeOOH, $BiVO_4$/NiOOH, $BiVO_4$/FeOOH/NiOOH and $BiVO_4$/NiOOH/FeOOH photoanodes and Cu_2O, Cu_2O/CuO, Cu_2O/CuO/TiO_2 and CuO photocathodes. (b and d) Chronoamperometry (*j vs. t*) measurements performed at 1.23 V *vs.* RHE for the $BiVO_4$ photoanodes and 0 V *vs.* RHE for the Cu_2O photocathodes tested in 0.1 M Na_2SO_4 (pH 6) in AM 1.5 G equipped illumination source with a power intensity of 100 mW cm^{-2}.

current density of ~2 mA cm^{-2} throughout the test without any significant degradation. Similarly, the Cu_2O/CuO/TiO_2 photocathode was stable throughout the measurement and retained the current density of −1.59 mA cm^{-2}. On the other hand, the bare Cu_2O photocathode was unstable in the photostability measurement test, as shown in Fig. S5(b).†

To further understand the kinetics of the PEC water splitting and the performance of the photoelectrodes, an electrochemical impedance spectroscopy (EIS) analysis was performed in a three-electrode configuration under illumination. The EIS analysis in Fig. 6 is shown in the form of a Nyquist plot from which the equivalent circuit can be constructed, which provides insights into the electrode and electrolyte interface. The Randles–Ershel fitting model was used in this study in which R_s is the series resistance, C_{PE} is the constant phase element accounted for the capacitance of the Helmholtz

Table 1 Tabulation of the PEC parameters of $BiVO_4$ photoanodes and Cu_2O photocathodes

Photoanode	Current density at 1.23 V *vs.* RHE (mA cm^{-2})	Onset potential (V *vs.* RHE)	Charge transfer resistance R_{ct} (Ω)
$BiVO_4$	0.65 mA cm^{-2}	0.46 V	1531 Ω
$BiVO_4$/FeOOH	1.24 mA cm^{-2}	0.43 V	1115 Ω
$BiVO_4$/NiOOH	0.91 mA cm^{-2}	0.42 V	1032 Ω
$BiVO_4$/FeOOH/NiOOH	1.81 mA cm^{-2}	0.45 V	876.9 Ω
$BiVO_4$/NiOOH/FeOOH	2.05 mA cm^{-2}	0.40 V	627 Ω
Photocathode	**Current density at 0 V *vs.* RHE (mA cm^{-2})**	**Onset potential (V *vs.* RHE)**	**Charge transfer resistance R_{ct} (Ω)**
Cu_2O	−0.62 mA cm^{-2}	0.37 V	1280 Ω
CuO	−0.81 mA cm^{-2}	0.44 V	935.8 Ω
Cu_2O/CuO	−1.26 mA cm^{-2}	0.73 V	848.5 Ω
Cu_2O/CuO/TiO_2	−1.61 mA cm^{-2}	0.75 V	407.5 Ω

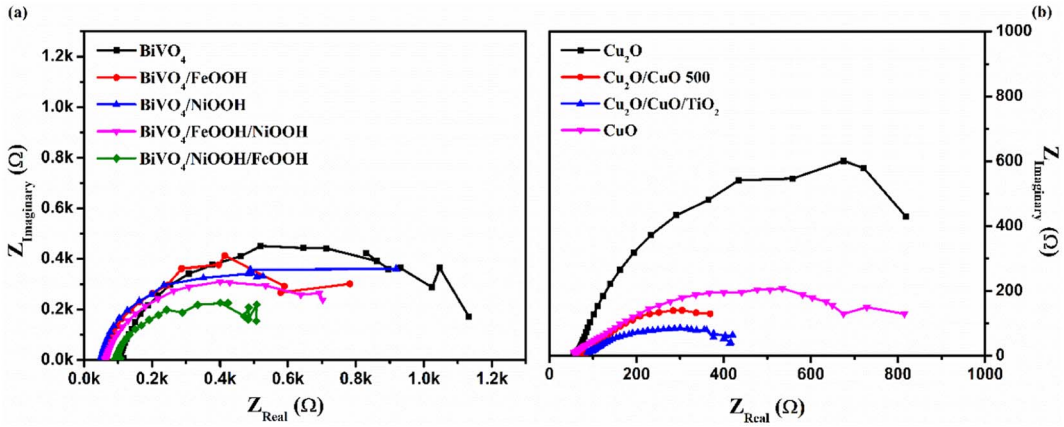

Fig. 6 Electrochemical impedance spectra (EIS) of (a) $BiVO_4$, $BiVO_4$/FeOOH, $BiVO_4$/NiOOH, $BiVO_4$/FeOOH/NiOOH and $BiVO_4$/NiOOH/FeOOH photoanodes and (b) Cu_2O, Cu_2O/CuO, Cu_2O/CuO/TiO_2 and CuO photocathodes tested in 0.1 M Na_2SO_4 (pH 6) in AM 1.5 G equipped illumination source with a power intensity of 100 mW cm^{-2}.

layer from the electrode and electrolyte interface, and R_{ct} is the charge transfer resistance across the interface.

Fig. 6(a) shows the EIS plot of $BiVO_4$ and co-catalyst-loaded $BiVO_4$ nanostructured photoanodes measured at 1.23 V *vs.* RHE. In the EIS spectra, the smaller semicircle corresponds to R_s and the larger semicircle corresponds to R_{ct}. Upon addition of the co-catalysts, a significant reduction in the charge transfer resistance was observed. The smaller R_{ct} value signifies an efficient charge transfer between the semiconductor–electrolyte interfaces. It was also observed that R_{ct} further decreases for the dual-cocatalyst loaded $BiVO_4$ nanostructured photoanode, compared to the mono co-catalyst counterpart. The $BiVO_4$/NiOOH/FeOOH photoanode exhibited the R_{ct} value of 627 Ω, which is lower than that for the bare $BiVO_4$ (1531 Ω). The result proved that the first layer co-catalyst aids in minimizing the surface defects and recombination, and the second layer co-catalyst helps in boosting the kinetics of OER. On the other hand, the EIS spectra of Cu_2O and the Cu_2O-modified photocathodes are shown in Fig. 6(b), which was measured at 0 V *vs.* RHE. The value of R_{ct} decreased in the order of Cu_2O > CuO > Cu_2O/CuO > Cu_2O/CuO/TiO_2. The extracted EIS spectra values also support the photocurrent density values observed from the LSV response. The TiO_2-protected Cu_2O/CuO photocathode has the lowest charge transfer resistance of 407.5 Ω, which is lower than that of the bare Cu_2O (1280 Ω). The constructed equivalent circuit of the photoanode and photocathode is shown in Fig. S4 in the ESI.†

Furthermore, Mott–Schottky (MS) analysis was carried for $BiVO_4$ and Cu_2O photoelectrodes under dark condition at 1 kHz frequency. The MS plots are used to calculate the flat band potential (E_{FB}) and carrier density. Fig. 7(a) shows the MS plots of the $BiVO_4$ nanostructured photoanodes, which exhibit positive slopes, indicating the intrinsic nature of the n-type behavior. The E_{FB} value of the bare $BiVO_4$ and $BiVO_4$/NiOOH/FeOOH photoanode was estimated to be 0.40 V and 0.41 V *vs.* RHE, respectively. The cathodic shift of E_{FB} for the latter is correlated to the significant reduction in the overpotential of OER caused by the FeOOH and NiOOH co-catalysts. The carrier density was extracted using the slope of the obtained MS plots and the values are summarized in Table 2. The higher carrier concentration means the photoanode/photocathode requires a low overpotential to initiate the charge transfer reaction,

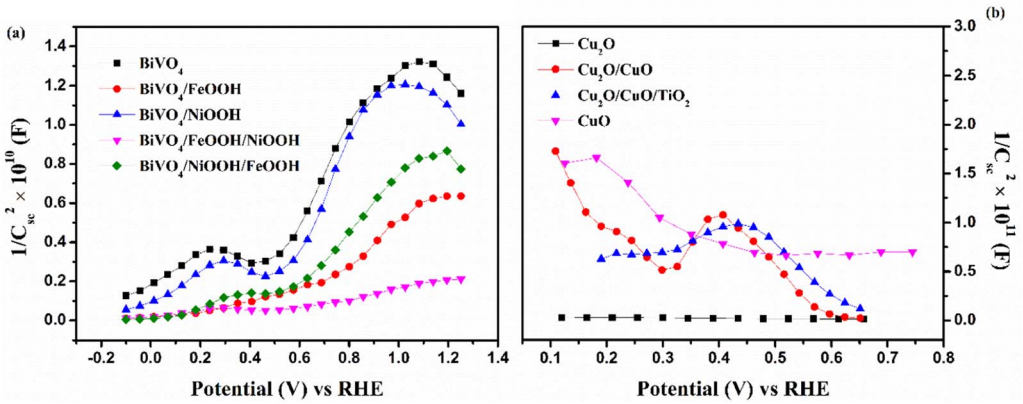

Fig. 7 Mott–Schottky plots of (a) $BiVO_4$, $BiVO_4$/FeOOH, $BiVO_4$/NiOOH, $BiVO_4$/FeOOH/NiOOH and $BiVO_4$/NiOOH/FeOOH photoanodes and (b) Cu_2O, Cu_2O/CuO, Cu_2O/CuO/TiO_2 and CuO photocathodes tested in 0.1 M Na_2SO_4 (pH 6) at 1 kHz under dark conditions.

Table 2 Tabulation of the PEC parameters of $BiVO_4$ photoanodes and Cu_2O photocathode

Photoanode	Flat band potential (E_{FB}) (V *vs.* RHE)	Carrier density (cm^{-3})
$BiVO_4$	0.40 V	6.129×10^{20}
$BiVO_4$/FeOOH	0.44 V	1.327×10^{21}
$BiVO_4$/NiOOH	0.43 V	5.249×10^{21}
$BiVO_4$/FeOOH/NiOOH	0.42 V	6.025×10^{21}
$BiVO_4$/NiOOH/FeOOH	0.41 V	8.561×10^{21}
Photocathode	**Flat band potential (E_{FB}) (V *vs.* RHE)**	**Carrier density (cm^{-3})**
Cu_2O	0.51 V	-1.218×10^{20}
CuO	0.57 V	-1.067×10^{20}
Cu_2O/CuO	0.62 V	-3.129×10^{20}
Cu_2O/CuO/TiO_2	0.64 V	-8.122×10^{20}

which is evident from the low charge transfer resistance obtained in the EIS spectra and the highest current density of the $BiVO_4$/NiOOH/FeOOH photoanode and Cu_2O/CuO/TiO_2 photocathode obtained in the LSV spectra. Fig. 7(b) shows the MS plot of the Cu_2O photocathodes, which shows the typical p-type behavior manifested as the negative slope. The MS result of the bare Cu_2O yielded the E_{FB} value of 0.51 V *vs.* RHE. The E_{FB} of 0.64 V *vs.* RHE was obtained for the Cu_2O/CuO/TiO_2 photocathode, which is more anodic than the bare Cu_2O, implying the potential of the heterojunction and protective layer in minimizing the surface defects.

3.3 Tandem PEC cell analysis

In order to analyze the viability of the proposed tandem cell, the absolute LSV responses of the $BiVO_4$ photoanodes and Cu_2O photocathodes are plotted to find the intersecting point, which provides the operating voltage and current density based on the PEC activity of the individual photoelectrodes. Fig. 8 shows the overlay plot of the absolute LSV responses of the $BiVO_4$/NiOOH/FeOOH *vs.* Cu_2O/CuO/TiO_2 tandem PEC cells. The overlay curve provided the operating photocurrent density of 0.344 mA cm^{-2} at the operating voltage of 0.51 V *vs.* RHE for the $BiVO_4$/NiOOH/FeOOH *vs.* Cu_2O/CuO/TiO_2 tandem cell. In the tandem cell measurement, the photoanode was placed on top of the photocathode for which a slight reduction in the operating current was identified as 0.202 mA cm^{-2} at 0.42 V *vs.* RHE for $BiVO_4$/NiOOH/FeOOH filtered with the Cu_2O/CuO/TiO_2 tandem cell. The tabulation of the operating points of the constructed tandem cell is provided in Table S3 in the ESI.† This intersection point provides us with the actual maximum limit of the proposed tandem PEC cell. The non-zero operating current density hints at the possibility of unassisted operation of the tandem PEC cell. The calculated solar-to-hydrogen (STH) conversion efficiency for the $BiVO_4$/NiOOH/FeOOH–Cu_2O/CuO/TiO_2 tandem cell was 0.27% using eqn (1.1) in the ESI.†

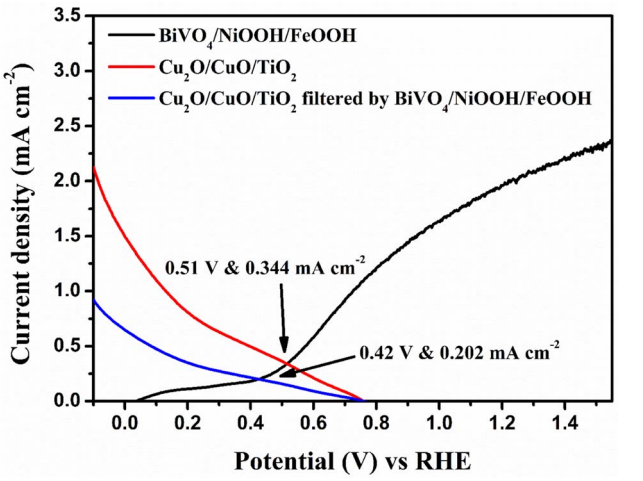

Fig. 8 Overlay of the absolute LSV responses of $BiVO_4$, $BiVO_4$/NiOOH/FeOOH, Cu_2O and Cu_2O/CuO/TiO_2 to find the operating point of the tandem cell.

The tandem cell was constructed using $BiVO_4$ as the top and Cu_2O as the bottom, as shown in Fig. S6 in the ESI.† We compared the performance of $BiVO_4$ *vs.* Cu_2O and $BiVO_4$/NiOOH/FeOOH *vs.* Cu_2O/CuO/TiO_2 tandem cells using two-electrode LSV analysis. Fig. 9(a) shows the LSV response under the AM1.5 G equipped illumination source with a power intensity of 100 mW cm^{-2}. The representative $BiVO_4$/NiOOH/FeOOH *vs.* Cu_2O/CuO/TiO_2 tandem cell produced an unassisted photocurrent density of 0.201 mA cm^{-2} at zero bias, whereas the bare $BiVO_4$ *vs.* Cu_2O produced a photocurrent density of 25.4 μA cm^{-2} at zero bias. The result suggested the potential of the co-catalyst loading in the photoanode side and heterojunction formation in the photocathode side upon enhancement of the PEC performance. Finally, the unassisted photostability tests were performed for both tandem cell structures for 3000 seconds, as shown in Fig. 9(b). The bare tandem cells provided negligible current density under illumination. This is due to the sluggish water splitting reaction kinetics and photocorrosion of the photocathode. For the $BiVO_4$/NiOOH/FeOOH *vs.* Cu_2O/CuO/TiO_2 tandem cell, the current density spiked to 0.32 mA cm^{-2} and the current density became constant after 50 seconds, with a stable current density of 0.187 mA cm^{-2}. The synergic effect of NiOOH/FeOOH on lowering the overpotential of the $BiVO_4$ nanostructure and the double protection of Cu_2O by CuO/TiO_2 enhanced the unassisted current density and ensured the stable operation of the tandem cell. The comparison of the tandem PEC cell with our previous works and the recent literature are tabulated in Table 3.

3.4 Post-PEC test characterization

XRD patterns of the photoanode and photocathode after the PEC test are shown in Fig. 10. The XRD patterns were recorded after the tandem PEC cell measurements, such as LSV and stability test. The XRD patterns of the $BiVO_4$/NiOOH/FeOOH photoanode were well indexed with JCPDS card no. 014-06888, as shown in Fig. 10(a), both before and after the PEC test. No shift in the peaks or appearance of new peaks was found for the

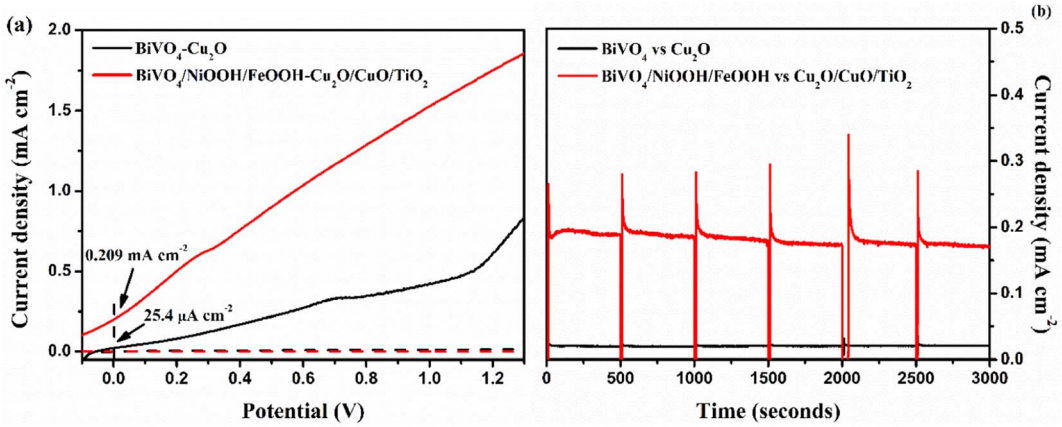

Fig. 9 (a) Two-electrode LSV responses, (b) stability tests (*j vs. t*) of $BiVO_4$ *vs.* Cu_2O and $BiVO_4$/FeOOH/NiOOH *vs.* Cu_2O/CuO/TiO_2 tandem cell tested in 0.1 M Na_2SO_4 (pH 6) in AM 1.5 G equipped illumination source with a power intensity of 100 mW cm^{-2}. The chopping of light was carried out every 500 seconds.

photoanode after the PEC tests, demonstrating the high stability of the $BiVO_4$/NiOOH/FeOOH photoanode. There was only a minor decrease in the intensity of the XRD pattern obtained after PEC testing, which could be due to different amounts used in the sample preparation. Similarly, the XRD patterns of the Cu_2O/CuO/TiO_2 photocathode obtained before and after PEC measurements are shown in Fig. 10(b). There is no significant change in the XRD peak positions and no new peaks appeared after the PEC test, which implied the stable nature of the photocathodes as a result of the CuO and TiO_2 protective layers.

Table 3 PEC performance comparison of various similar tandem PEC cells reported in the literature

Photoanode	Photocathode	Electrolyte	pH	Current density of the tandem cell	References
$BiVO_4$/Co-Pi	Cu_2O/Al:ZnO/TiO_2/RuO_x	0.5 M Na_2SO_4 + 0.09 KH_2PO_4 + K_2HPO_4	6	0.25 mA cm^{-2}	36
$BiVO_4$/TiO_2/FeOOH	Cu_2O	0.2 M phosphate buffer	8	0.12 mA cm^{-2}	24
W–$BiVO_4$/Co-Pi	$CuBi_2O_4$/CdS/TiO_2/RuO_x	0.3 M K_2SO_4 + 0.2 M phosphate buffer	6.8	0.1 mA cm^{-2}	37
$BiVO_4$/Co–Bi	$CuBi_2O_4$/Co–Bi	0.5 M borate buffer	9.2	0.036 mA cm^{-2}	38
$BiVO_4$	Au/Cu_2O/H:$Ti_3C_3T_x$	1 M Na_2SO_4	5	−0.45 mA cm^{-2}	39
Mo–$BiVO_4$/Co-Pi	$CuBi_2O_4$/Pt	0.1 M potassium phosphate buffer	7	0.15 mA cm^{-2}	40
Mo–$BiVO_4$/TiO_2/FeOOH	Cu_2O/TiO_2/MoS_2	0.1 M Na_2SO_4	6	0.0653 mA cm^{-2}	34
Mo–$BiVO_4$/C/FeOOH	Cu_2O/C/MoS_2	0.1 M Na_2SO_4	6	0.107 mA cm^{-2}	35
$BiVO_4$/NiOOH/FeOOH	Cu_2O/CuO/TiO_2	0.1 M Na_2SO_4	6	0.187 mA cm^{-2}	This work

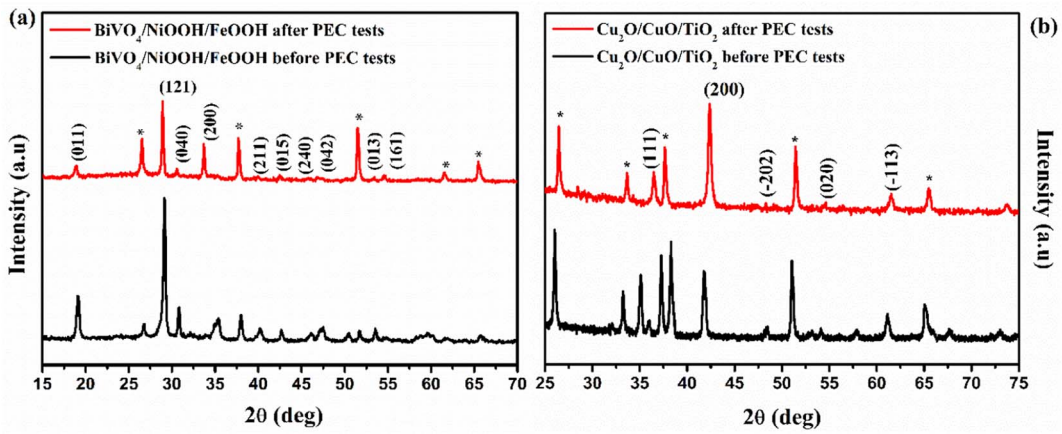

Fig. 10 XRD pattern obtained before and after PEC measurements of the (a) $BiVO_4$/NiOOH/FeOOH photoanode and (b) Cu_2O/CuO/TiO_2 photocathode.

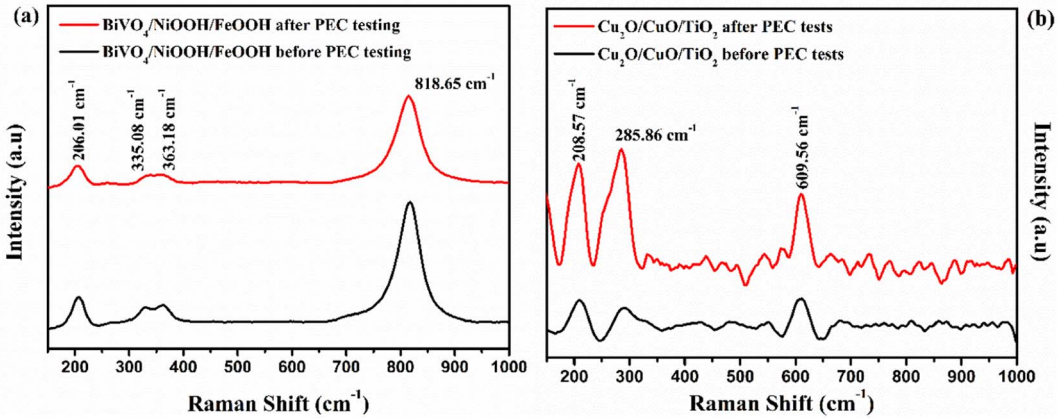

Fig. 11 Raman spectra obtained before and after PEC testing of (a) the $BiVO_4$/NiOOH/FeOOH photoanode and (b) Cu_2O/CuO/TiO_2 photocathode.

Raman spectra were obtained for the $BiVO_4$/NiOOH/FeOOH photoanode and Cu_2O/CuO/TiO_2 photocathodes, and are illustrated in Fig. 11(a) and (b), respectively. The Raman spectra of the photoanode showed that no significant change in peak position or appearance of new peaks occurred after PEC measurement. Similarly, in the Raman spectra of the photocathode before and after PEC testing, the photocathode exhibited two major characteristic peaks of Cu_2O and CuO at 208.57 cm^{-1} and 285.86 cm^{-1}, respectively. The major peak at 208.57 cm^{-1} was the characteristic second order Raman peak of cubic Cu_2O, and the peak at 285.86 cm^{-1} was the characteristic peak of CuO. The Raman result also confirmed the stable nature of the photoelectrodes after the PEC tests.

4. Conclusion

A simple and economical strategy for boosting the PEC performance of the $BiVO_4$ and Cu_2O tandem cell was reported. The tandem cell consisted of the nanostructured $BiVO_4$/NiOOH/FeOOH photoanode and heterojunction Cu_2O/CuO/TiO_2 photocathode, which exhibited improved PEC performance compared to reference tandem structures with single component counterparts. The formation of the $BiVO_4$ nanostructures increased the surface active area. The co-catalyst NiOOH facilitated the separation of charge carriers from $BiVO_4$, and FeOOH facilitated the transfer of charge carriers to the surface of the photoelectrode. The representative photoanode and photocathode produced a photocurrent density of 2.05 mA cm^{-2} at 1.23 V *vs.* RHE and 1.61 mA cm^{-2} at 0 V *vs.* RHE, respectively. The thermal oxidation of Cu_2O *in situ* formed a Cu_2O/CuO heterojunction, which efficiently separated the photogenerated charges due to favorable downward band bending. The $BiVO_4$/NiOOH/FeOOH *vs.* Cu_2O/CuO/TiO_2 model tandem cell produced an unassisted current density of 0.185 mA cm^{-2}, which is equivalent to 0.22% STH efficiency. The tandem cell was stable during the testing duration of 3000 second, and the post-XRD and Raman characterizations showed negligible structural changes in the photoelectrodes.

Author contributions

Sitaaraman S. R.: methodology, writing – original draft. Nirmala Grace A.: funding acquisition, validation. Jiefang Zhu: revising draft, validation. Raja Sellappan: methodology, writing – original draft, funding acquisition, validation.

Conflicts of interest

The authors declare that they have no known competing financial interests or personal relationships that could have appeared to influence the work reported in this paper.

Acknowledgements

This work was supported by DST – SERB, Government of India. The authors are grateful to DST – SERB project EMR/2017/001185 for the financial support.

References

1 A. Fujishima and K. Honda, *Nature*, 1972, **238**, 37–38.
2 P. Chatterjee, M. S. K. Ambati, A. K. Chakraborty, S. Chakrabortty, S. Biring, S. Ramakrishna, T. K. S. Wong, A. Kumar, R. Lawaniya and G. K. Dalapati, *Energy Convers. Manag.*, 2022, **261**, 115648.
3 B. D. Sherman, M. V. Sheridan, K. R. Wee, S. L. Marquard, D. Wang, L. Alibabaei, D. L. Ashford and T. J. Meyer, *J. Am. Chem. Soc.*, 2016, **138**, 16745–16753.
4 Gurudayal, D. Sabba, M. H. Kumar, L. H. Wong, J. Barber, M. Grätzel and N. Mathews, *Nano Lett.*, 2015, **15**, 3833–3839.
5 A. M. K. Fehr, A. Agrawal, F. Mandani, C. L. Conrad, Q. Jiang, S. Y. Park, O. Alley, B. Li, S. Sidhik, I. Metcalf, C. Botello, J. L. Young, J. Even, J. C. Blancon, T. G. Deutsch, K. Zhu, S. Albrecht, F. M. Toma, M. Wong and A. D. Mohite, *Nat. Commun.*, 2023, **14**, 1–12.
6 Q. Chen, G. Fan, H. Fu, Z. Li and Z. Zou, *Adv. Phys.: X*, 2018, **3**, 863–884.

7 M. S. Prévot and K. Sivula, *J. Phys. Chem. C*, 2013, **117**, 17879–17893.
8 C. Jiang, S. J. A. Moniz, A. Wang, T. Zhang and J. Tang, *Chem. Soc. Rev.*, 2017, **46**, 4645–4660.
9 K. Zhang, M. Ma, P. Li, D. H. Wang and J. H. Park, *Adv. Energy Mater.*, 2016, **6**, 1600602.
10 Y. Liu, W. Qiu, G. He, K. Wang, Y. Wang, L. Chen, Q. Wu, W. Li and J. Li, *J. Phys. Chem. C*, 2022, **126**, 15596–15605.
11 L. Wang, Z. Liu, X. Xu, Y. Jia, Q. Mei, F. Ding, J. Peng and Q. Wang, *ACS Appl. Energy Mater.*, 2022, **5**, 6383–6392.
12 K. Chen, R. Wang, Q. Mei, F. Ding, H. Liu, G. Yang, B. Bai and Q. Wang, *Applied Catalysis B: Environment and Energy*, 2024, **344**, 123670.
13 J. Zhang, X. Wei, J. Zhao, Y. Zhang, L. Wang, J. Huang and H. She, *Chem. Eng. J.*, 2023, **454**, 140081.
14 X. Wei, J. Zhang, L. Wang, Y. Bai, J. Huang, H. She and Q. Wang, *Chem. Eng. J.*, 2024, **482**, 149114.
15 S. Majumder, N. D. Quang, T. T. Hien, N. D. Chinh, N. M. Hung, H. Yang, C. Kim and D. Kim, *Appl. Surf. Sci.*, 2021, **546**, 149033.
16 S. S. Kalanur and H. Seo, *J. Catal.*, 2022, **410**, 144–155.
17 Y. Liu, B. R. Wygant, O. Mabayoje, J. Lin, K. Kawashima, J. H. Kim, W. Li, J. Li and C. Buddie Mullins, *ACS Appl. Mater. Interfaces*, 2018, **10**, 12639–12650.
18 D. K. Lee and K. S. Choi, *Nat. Energy*, 2018, **3**, 53–60.
19 D. Jeong, W. Jo, J. Jeong, T. Kim, S. Han, M. K. Son and H. Jung, *RSC Adv.*, 2022, **12**, 2632–2640.
20 Y. Yang, D. Xu, Q. Wu and P. Diao, *Sci. Rep.*, 2016, **6**, 35138.
21 P. Wang, Z. Liu, C. Han, X. Ma, Z. Tong and B. Tan, *J. Nanopart. Res.*, 2021, **23**, 268.
22 C. Y. Toe, J. Scott, R. Amal and Y. H. Ng, *J. Photochem. Photobiol., C*, 2019, **40**, 191–211.
23 Y. Wang, S. Cao, Y. Huan, T. Nie, Z. Ji, Z. Bai, X. Cheng, J. Xi and X. Yan, *Appl. Surf. Sci.*, 2020, **526**, 146700.
24 X. Yin, Q. Liu, Y. Yang, Y. Liu, K. Wang, Y. Li, D. Li, X. Qiu, W. Li and J. Li, *Int. J. Hydrogen Energy*, 2019, **44**, 594–604.
25 W. Zhang, J. Ma, L. Xiong, H. Y. Jiang and J. Tang, *ACS Appl. Energy Mater.*, 2020, **3**, 5927–5936.
26 J. Wei, C. Zhou, Y. Xin, X. Li, L. Zhao and Z. Liu, *New J. Chem.*, 2018, **42**, 19415–19422.
27 I. R. Hamdani and A. N. Bhaskarwar, *Sol. Energy Mater. Sol. Cells*, 2022, **240**, 111719.
28 P. P. Kunturu and J. Huskens, *ACS Appl. Energy Mater.*, 2019, **2**, 7850–7860.
29 X. Deng, G. C. Wilkes, A. Z. Chen, N. S. Prasad, M. C. Gupta and J. J. Choi, *J. Phys. Chem. Lett.*, 2017, **8**, 3206–3210.
30 H. Luo, C. Liu, Y. Xu, C. Zhang, W. Wang and Z. Chen, *Int. J. Hydrogen Energy*, 2019, **44**, 30160–30170.
31 H. L. S. Santos, P. G. Corradini, M. A. S. Andrade and L. H. Mascaro, *J. Solid State Electrochem.*, 2020, **24**, 1899–1908.
32 A. Galembeck and O. L. Alves, *Thin Solid Films*, 2000, **365**, 90–93.
33 M. Balık, V. Bulut and I. Y. Erdogan, *Int. J. Hydrogen Energy*, 2019, **44**, 18744–18755.
34 S. R. Sitaaraman, A. Nirmala Grace and R. Sellappan, *RSC Adv.*, 2022, **12**, 31380–31391.
35 S. Srinivasa, R. Raghavan, N. G. Andrews and R. Sellappan, *Catalysts*, 2023, **13**, 1–15.
36 P. Bornoz, F. F. Abdi, S. D. Tilley, B. Dam, R. Van De Krol, M. Graetzel and K. Sivula, *J. Phys. Chem. C*, 2014, **118**, 16959–16966.
37 A. Song, P. Bogdanoff, A. Esau, I. Y. Ahmet, I. Levine, T. Dittrich, T. Unold, R. Van De Krol and S. P. Berglund, *ACS Appl. Mater. Interfaces*, 2020, **12**, 13959–13970.
38 Y. H. Lai, K. C. Lin, C. Y. Yen and B. J. Jiang, *Faraday Discuss.*, 2019, **215**, 297–312.
39 X. Fu, H. Chang, Z. Shang, P. Liu, J. Liu and H. Luo, *Chem. Eng. J.*, 2020, **381**, 122001.
40 J. H. Kim, A. Adishev, J. Kim, Y. S. Kim, S. Cho and J. S. Lee, *ACS Appl. Energy Mater.*, 2018, **1**, 6694–6699.